International Journal of Heat and Mass Transfer 115 (2017) 743–753

Contents lists available at ScienceDirect

International Journal of Heat and Mass Transfer

journal homepage: www.elsevier.com/locate/ijhmt

Prediction of steady-state freeze front position during 3D printing of microstructures

Abhishek Gannarapu, Prashanta Dutta, B. Arda Gozen *

School of Mechanical and Materials Engineering, Washington State University, Pullman, WA 99164-2920, USA

ARTICLE INFO

Article history:
Received 9 February 2017
Received in revised form 19 July 2017
Accepted 20 July 2017

Keywords:
Additive manufacturing
Freeze-front propagation
3D printing
Solidification
EGaIn

ABSTRACT

Additive manufacturing with alloys at micro and meso-scales is an emerging technology with applications in printed, flexible or conformable electronics, solar energy and biomedical science. Among various additive manufacturing techniques, the recently introduced 3D-freeze-printing technique has the potential to revolutionize printed circuits, sensors and conformal wearable electronics. In 3D-freeze-printing, low melting point alloys are dispensed through a micro-scale nozzle on a cooled substrate and frozen simultaneously to create three-dimensional structures. The quality of the 3D printed structures relies on a continuous liquid-to-solid phase change of the printed filamentary structures through the propagation of a freeze-front. Thus to achieve stable printing of complex 3D structures, the study of freeze-front position is critical. In this paper, we present a thermal model to predict the steady-state freeze-front position during the freeze-printing process. Thermal modeling can aid in predicting parameter dependent process response and help achieve robust 3D printing with high accuracy and high throughput. Owing to the disparate length scale and nature of materials, quasi 1D energy equations are developed to model the printed structures and dispensing nozzle, while 2D energy equations are used to model the heat transfer from the liquid alloy reservoir. A finite volume method with a modified variable time-step approach is used for the discretization of governing differential equations to find the freeze front. The validity of this model was experimentally tested for three cases: vertical printed structures with and without a connected nozzle and a horizontally printed structure with a connected nozzle. It was shown that the model predicted the freeze-front position with high accuracy for various substrate temperatures and process conditions.

1. Introduction

Additive manufacturing (AM) is emerging as an important manufacturing technology with increasing research and capital investment on materials, machinery, process control and modeling. It has received significant attention owing to its capability of fabricating geometrically complex and customizable products at various size scales. One of the key achievements of AM is its capability to print metals or alloys in micro-meso scale. This capability aided in technological advancements by transforming printed circuit boards [1] and flexible conformal devices [2] in 3D and realizing highly resolved, high-aspect ratio electrodes [3]. Thereupon, it enabled myriad applications in electronics [4], microelectromechanical systems (MEMS) [5], solar cell metallization [6], and biomedical applications [7]. Despite these advancements, complex integration of such devices is still very challenging. To realize the full potential of these applications, there is a significant need for research on metal/alloy AM methods at micro-meso scales towards enhancing their complex geometric capabilities and improve their quality. A recent report by IDA – Science and Technology Policy Institute [8] points out the importance of process control and modeling to ensure consistency and quality of printed structures in AM. As such, theoretical research and comprehensive modeling to understand the fundamental aspects of the metal/alloy additive manufacturing processes are critical.

In micro-meso scale, additive manufacturing can be broadly classified into discrete and continuous methods. In discrete methods, such as inkjet printing [9] or aerosol jet printing [10], the alloy inks or powdered nanoparticles are dispensed discretely (drop-by-drop) leading to non-uniform surface morphologies causing mechanical instability of the printed structures [9]. On the contrary, in continuous methods, such as direct-ink-writing [11], the liquid inks are dispensed directly in the desired 3D patterns to realize complex structures. Yet, the present direct writing techniques are either limited due to their slow speed [12] or complex material

* Corresponding author.
E-mail address: arda.gozen@wsu.edu (B.A. Gozen).

http://dx.doi.org/10.1016/j.ijheatmasstransfer.2017.07.092
0017-9310/

Nomenclature

C	specific heat
g	acceleration due to gravity
h	convective heat transfer coefficient
k	thermal conductivity of
L	length
Lh	latent heat of fusion of EGaIn
Nu	Nusselt number
Pr	Prandtl number
$\dot{q}$	Heat flux
$s(t)$	position of the freeze front
T	temperature

Greek symbols

ρ	density
v	kinematic viscosity
β	thermal expansion coefficient

Subscripts

air	air
cp	cold plate
D	diameter
EGaIn	gallium indium alloy
eq	equivalent
exp	exposed length
f	fusion
in	initial
l	liquid
m	melting point
o	previous time step
pr	printed
s	solid
steel	steel
still	still air
v	vertical length
x	local position
∞	ambient

preparation procedures wherein the alloy nanoparticles are treated with solvents to yield 3D-printable inks [13]. Moreover, most [11,13] of the techniques are either limited to 2D or need support structures to facilitate the printing of 3D structures. To address these issues, in our recent work [14], we demonstrated direct ink writing of a room temperature liquid alloy (eutectic alloy of gallium indium – EGaIn, melting point ~15 °C) in complex 3D geometries through a process referred to as 3D-freeze printing. Here, the structures are fabricated through simultaneous freezing of the alloy as it is printed. We have realized complex geometries such as non-vertical lines with wide angle range and freely suspending horizontal lines. To achieve robust 3D-freeze printing with high accuracy and high throughput, there is a need for detailed understanding of the fundamental mechanisms involved. The most critical aspect of 3D freeze-printing in this regard is the thermal mechanisms behind freezing of the printed liquid metal structures. The spatial and temporal behavior of the liquid-to-solid phase change need to be understood to achieve printing of structurally stable structures with reasonable throughputs. As such, thermal modeling would greatly aid in predicting parameter dependent process response and determining the workspace of stable printing. The primary challenge here is that there is only a very limited set of modeling studies in the literature looking into the heat transfer mechanisms in the size scales relevant to freeze printing, particularly in the domain of additive manufacturing.

Thermal models are used in other manufacturing techniques, such as laser assisted direct-ink-writing [13], where the metal inks are dispensed through a nozzle and simultaneously sintered using a high energy laser beam. In this work, Skylar-Scott et al. solved a one-dimensional heat equation to optimize the laser-to-nozzle distance. For additive manufacturing at larger scale, models have been developed to study the microstructural evolution of specific alloys such as Ti-6Al-4V [15] and to understand the effects of process parameters such as laser beam energy, powder or wire feed rate and tip velocity [16,17] on the printed alloys. Yet, to the best of our knowledge, a thermal model to understand the complete heat transfer mechanisms and the progression of liquid-to-solid phase change of the printed materials for micro-meso scale continuous metal additive manufacturing has not yet been reported. Such thermal models are critical towards predicting and improving the material, size scale and throughput related capabilities of small scale metal/alloy additive manufacturing in general.

In this paper, we present an experimentally validated-thermal model to study the steady-state characteristics of the freeze-printing of eutectic room temperature liquid metal alloy EGaIn. As stated above, for 3D structure formation, freeze-printing relies on a continuous liquid-to-solid phase change of the printed filamentary structures through the propagation of a freeze-front. We utilized finite volume method with a modified variable time step approach [18] to solve the governing differential equations. The prediction on freeze-point relies heavily on the accurate determination of the thermal conductivity of the printed metal in the solid and the liquid phase. To this end, we conducted experimental studies to characterize the metal thermal conductivity using the Wiedemann-Franz law [19]. We particularly studied the dependence of freeze front position on the cold plate temperature and validated the applicability of the model for different 3D geometries.

The rest of the paper is organized as follows: First, the details of the freeze printing process, the mathematical formulation for the freeze front study and the method for finding the convective heat transfer coefficient are explained. Second, experimental setup and methods of determining various critical parameters are described. Third, our finite volume based numerical models are presented for different cases. Finally, the results of the experimental validation studies and the associated discussions are provided.

2. Freeze-printing process

In the "3D Freeze-Printing [14]" method liquid metal alloys can be dispensed in complex 3D shapes as schematically shown in Fig. 1(a)–(c). The liquid alloy used in this study is a eutectic composition of gallium (78%) and indium (22%) (EGaIn) having a melting temperature of ~ 15°C. The liquid alloy is dispensed from a nozzle onto a substrate (hosted by a temperature controlled cold plate) whose temperature is maintained below the melting point of the alloy. By controlling the air pressure inside the syringe, liquid alloy can be continuously dispensed on the already printed structure as the nozzle translates in complex 3D paths. The printed structures maintain cylindrical shape owing to the spontaneous formation of a skin of gallium (II) oxide [20]. This nanostructured oxide skin [21,22] acts as an elastic membrane surrounding the liquid alloy inside. Alongside, the printed structure starts to freeze from the cold substrate generating a moving freeze-front providing

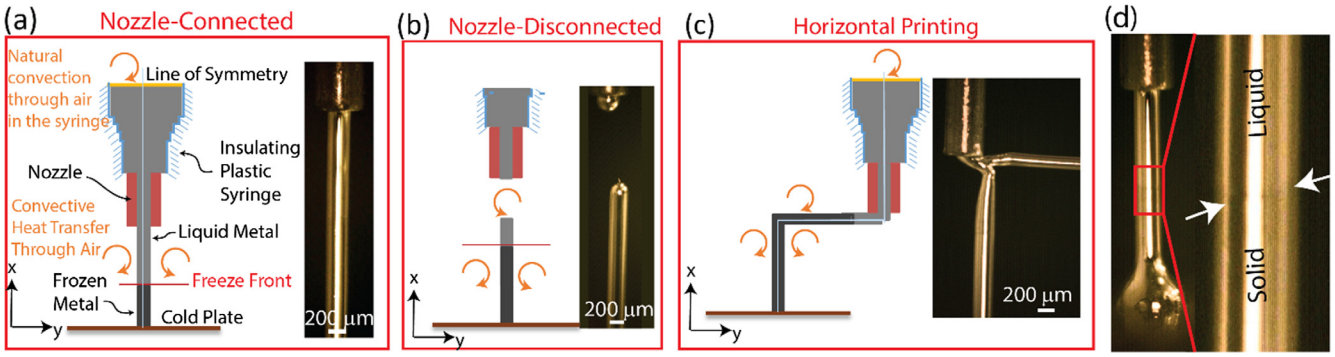

Fig. 1. Schematics and microscopy images of three different freeze-front (FF) propagation based additive manufacturing techniques: vertical printing (a) nozzle-connected and (b) nozzle-disconnected, (c) horizontal printing. (d) Microscopic image of the freeze-printed structure along with the propagation of the freeze front. The white arrows highlight the freeze-front.

higher structural stability than the oxide skin alone. By maintaining the structural stability of both the liquid and the solid portions while printing, complex 3D shapes can be realized. As the printing continues, the moving freeze front can be optically observed as shown in Fig. 1(d) (also see Supplementary Video). Once the desired dimensions are achieved, a high vacuum along with an accelerated translation motion of the stage is applied to disconnect the nozzle from the printed structure. The printed structures can be encapsulated in liquid precursors of thermosetting elastomers to realize flexible electronic applications [14].

3. Mathematical formulation for freeze front

We have considered three different scenarios for the freeze-printing process as shown in Fig. 1. The liquid alloy is dispensed from a thermally insulating plastic syringe through a metallic nozzle of micron scale opening. In the first (Fig. 1a) and second (Fig. 1b) cases, vertical structures are printed with connected and disconnected dispensing nozzle, while in the third (Fig. 1c) case horizontal structure is printed with the connected dispensing nozzle. As the metal/alloy is being dispensed out of the nozzle, the cold plate extracts heat from the printed structure generating a moving freeze front from the plate surface. This freeze front evolves from the substrate which is set at a temperature lower than the melting point of the alloy and propagates towards the nozzle with a decelerating rate as the temperature reaches solidification point. This leads to a two-phase phenomenon within the printed structure with time varying temperature gradients in solid and liquid phases with a moving freeze front. A steady state is achieved when the freeze front stagnates or the whole printed structure freezes.

3.1. Governing equations for temperature

In micro/meso scale freeze-printing system, the printed structure and the dispensing nozzle have micron size diameter, while the diameter of reservoir containing the liquid metal alloy is three to four orders higher. Hence, the heat transfer in the printed structures and the nozzle-metal system are modeled using an unsteady 1D conduction as

$$k_i \frac{\partial^2 T_i(x,t)}{\partial x^2} + h_x \frac{P_i}{A_i}(T_\infty - T_i) = \rho_i C_i \frac{\partial T_i(x,t)}{\partial t} \quad i = s, l, eq \tag{1}$$

Here, boundary effects due to convection are accounted as a distributed source term. The choice of local heat transfer coefficient h_x is described later in this section. This quasi 1-D approximation neglects temperature distribution in the radial direction, and is a very good assumption for highly (thermally) conductive materials and/or structures with much smaller radial dimension compared to the axial length [23]. On the other hand, the heat transfer in the syringe region is considered to be 2-D unsteady conduction.

$$k_l \frac{\partial^2 T_i(x,y,t)}{\partial x^2} + k_l \frac{\partial^2 T_i(x,y,t)}{\partial y^2} = \rho_l C_{EGaIn} \frac{\partial T_i(x,y,t)}{\partial t} \quad i = bulk \tag{2}$$

Other assumptions and simplifications made to develop the mathematical model are as follows

1. Temperature-dependent variations of liquid and solid thermal conductivities are neglected over the range of temperature considered (0–30 °C).
2. The variation in liquid and solid densities (~ 3% [24,25]) and heat capacities are neglected.
3. The liquid metal has a constant melting-freezing temperature (13 °C – determined experimentally (Section 4.3)).
4. The plastic syringe used to hold the liquid metal alloy is assumed to be insulating.
5. For vertical printing with connected nozzle and horizontal printing cases, heat conduction in the nozzle region is through the metallic nozzle and the liquid metal alloy inside the nozzle. Hence, equivalent thermal conductivity is defined within the region by assuming thermal resistances of the nozzle and liquid metal to be in parallel.
6. For the nozzle-liquid metal system, the thermal contact resistance between the two materials is neglected. Within the same region, the equivalent density and specific heat are determined based on the volume fraction as

$$\rho_{eq} = \frac{(\rho_{EGaIn} V_{EGaIn} + \rho_{steel} V_{steel})}{V_{EGaIn} + V_{steel}} \tag{3.1}$$

$$C_{eq} = \frac{(C_{EGaIn} V_{EGaIn} + C_{steel} V_{steel})}{V_{EGaIn} + V_{steel}} \tag{3.2}$$

3.2. Auxiliary conditions

3.2.1. Case A: Vertical printing with connected nozzle

For the vertical nozzle connected case as shown in Fig. 1(a), the solid-liquid interface energy balance equation takes the form as

$$k_s \frac{\partial T_s}{\partial x}\bigg|_{x=s(t)} - k_l \frac{\partial T_l}{\partial x}\bigg|_{x=s(t)} = \rho_{EGaIn} L h_f \frac{\partial s(t)}{\partial t} \tag{4}$$

while the initial temperature of the whole printing system is taken to be that of the chamber temperature given by

$$T_l(x,0) = T_{eq}(x,0) = T_{bulk}(x,y,0) = T_{in} \quad x \geqslant 0 \tag{5}$$

$$s(0) = 0 \tag{5.2}$$

The boundary conditions are defined at the interfaces between the solid-liquid printed structure, liquid-nozzle interface and the nozzle-bulk interface. Alongside, we have the cold plate temperature condition at the substrate surface and the mixed boundary condition at the top surface of the bulk. These conditions are given by

$$T_s(0,t) = T_{cp} \tag{6.1}$$

$$T_s(s(t),t) = T_l(s(t),t) = T_m \tag{6.2}$$

$$k_l \frac{\partial T_l}{\partial x}\bigg|_{x=L_{pr}} = k_{eq} \frac{\partial T_{eq}}{\partial x}\bigg|_{x=L_{pr}} \tag{6.3}$$

$$k_{eq} \frac{\partial T_{eq}}{\partial x}\bigg|_{x=L_{exp}} = k_l \frac{\partial T_l}{\partial x}\bigg|_{x=L_{exp}} \tag{6.4}$$

$$\frac{\partial T_{bulk}(x, r^x_{bulk}, t)}{\partial y} = 0 \quad x > L_{exp} \tag{6.5}$$

$$\dot{q}(L_{bulk}) = h_{still}(T_\infty - T_b) \tag{6.6}$$

3.2.2. Case B: Vertical printing with disconnected nozzle

For the disconnected case as shown in Fig. 1(b), the nozzle and the bulk are disconnected from the printed structure and hence the heat transfer is only through the printed structure. The interface energy balance equation is same as that of the connected case and is given by Eq. (4).

The initial conditions are given by

$$T_l(x,0) = T_{in} \quad x > 0 \tag{7.1}$$

$$s(0) = 0 \tag{7.2}$$

The boundary conditions are such that at the disconnected end of the printed structure, we have a mixed boundary condition as presented below

$$T_s(0,t) = T_{cp} \tag{8.1}$$

$$T_s(s(t),t) = T_l(s(t),t) = T_m \tag{8.2}$$

$$k_l \frac{\partial T_l}{\partial x}\bigg|_{x=L_{pr}} = h_x \frac{P}{A}(T_l(L_{pr},t) - T_\infty) \tag{8.3}$$

3.2.3. Case C: Horizontal printing

The boundary conditions for horizontal line printing are the same as described in Section 3.2.1. The only difference would be in the local convective heat transfer coefficient, where the characteristic length for the horizontal cylinder is the diameter of the cylinder.

3.3. Convective heat transfer coefficient

In all three representative cases, the proper selection of convective heat transfer coefficient is very important for the solution of these problems. The convective heat transfer coefficient is found from the Nusselt number for the horizontal and vertical printed section as

$$h_D = \frac{Nu_D k_{air}}{L_v} \quad x \geqslant L_v \tag{9}$$

$$h_x = \frac{Nu_x k_{air}}{x} \quad 0 \leqslant x \leqslant L_v \;\&\; L_{pr} \leqslant x \leqslant L_{exp} \tag{10}$$

Here L_v is the length of the vertical leg over which we print our horizontal structure. L_{exp} is the distance from the cold plate to the end of the nozzle that is exposed to convective heating. This average Nusselt number for horizontal cylinders is given by [26]

$$Nu_D = \left(0.36 + \frac{0.518 Ra_D^{1/4}}{[1 + (0.559/Pr_{air})^{9/16}]^{4/9}}\right) \tag{11}$$

where the Rayleigh number is given as

$$Ra_j = \left(\frac{g\beta j^3 \rho_{air} C_{air}}{\upsilon_{air} k_{air}}\right)(T_i(x,t) - T_\infty(x,t)) \quad i = s,l,eq \quad j = x,D \tag{12}$$

The local Nusselt number (Nu_x) for a vertical cylinder is given by [27]

$$Nu_x = \left(A + 0.75\left(\frac{Ra_x}{4(0.609 + 1.221(Pr_{air})^{0.5} + 1.238 Pr_{air})}\right)^{0.25}\right) \tag{13}$$

The constant A is added to account for shape factors and deviations from the vertical flat plate at low Rayleigh numbers such as in the present case, as no correlation for Nusselt's number at low Ra is available for vertical cylinders [28]. The value of A in Eq. (13) is determined experimentally through a Nelder-Mead simplex optimization algorithm such that the minimal error between the model and the experimental results are obtained in case C for substrate temperature of 0 °C, among all the different printed distances (line heights) tested. The value of 2.7 determined through this method is then used for all the other cases studied.

4. Experimental methods

4.1. Freeze-printing setup

The printing system broadly comprises the motion system, dispensing system and the cold plate as shown in Fig. 2. The motion is controlled by three lead screw driven stages (Opto Sigma SGSP33-100). The Z-stage is mounted vertically and carries a 30 cc syringe while the X and Y stages are stacked perpendicularly on a horizontal plane. The X-Y stages host a thermoelectric cold plate (TE Tech Inc. CP-121) which is capable of controlling the substrate temperature ranging from −20 to 70 °C through a cold plate controller. The 30 cc syringe is filled with EGaIn up to a height of 40 mm and the dispensing pressure inside it is controlled by a high precision dispensing system (Nordson EFD Inc. Ultimus V). The motion

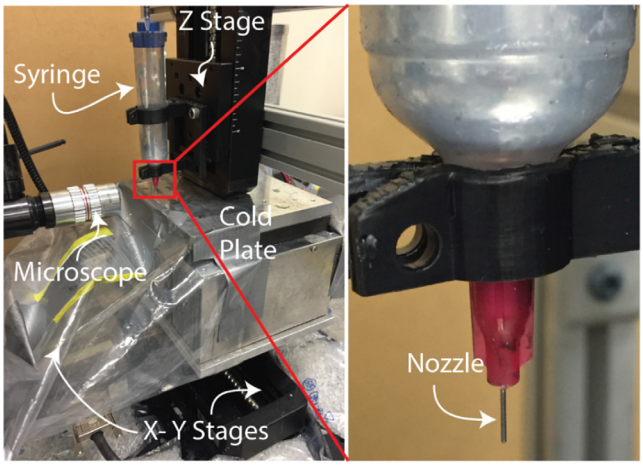

Fig. 2. The freeze printing system.

system, cold plate and the dispensing system is interfaced through data acquisition unit (NI PXIe-6363) and controlled by a LabView program. The entire system is operated inside a closed humidity control chamber having passive desiccants and intermittently flushed with dry air to maintain relative humidity lower than 15%. This is to prevent condensation at lower temperatures (below 2 °C). The cold plate's heat sink is isolated from the chamber through a ducting system around the inlet and outlet of the sink to prevent temperature rise inside the chamber. The printing process is continuously observed using a microscope system (Navitar UltraZoom 6.5x Microscope Tube coupled with Motic 5X Objective) which is attached to manual stages.

4.2. Temperature and freeze front measurements

To understand the thermal aspects of our printing process, we studied the spatial evolution and propagation of the freeze front on vertically and horizontally printed lines. To prepare the substrate surfaces, an adhesive double sided Scotch Tape is coated with a thin layer of EGaIn. Once this thin layer freezes, it acts as a freeze initiator for the printed structures, preventing supercooling which is commonly observed in gallium alloys [29]. Further, the thin layer helps the printed structure adhere to the surface strongly preventing mechanical instability while printing. The temperature of the film is measured by a thermistor (TE Tech Inc. MP-3176) placed directly on the film surface using thermal paste. The thermistor uses a 5k-1 TS-141 curve with a control range from −40 °C to 70 °C and has an accuracy of ±1°C. We studied the freeze front motion at 0 °C and 5 °C cold plate temperature on vertical lines ranging from 3 mm to 14 mm height with a 250 μm nozzle diameter. The freeze front stagnation height (steady state freeze front position) for different line lengths before and after nozzle disconnection is recorded through in-situ optical microscopy measurements. At each line length and cold plate temperature, we conducted 5 different tests and the average stagnation height was noted with a variation of <4%.

For the horizontal printing study, we printed structures at 0 °C that consists of two vertical lines of 5 mm height connected with horizontal lines of varying lengths. To this end, we first print the vertical legs and disconnect it from the nozzle. Then we connect the vertical legs with a new droplet of EGaIn and traverse horizontally yielding a structure such as the one shown in Fig. 1(c). While printing horizontally, the freeze front starts to propagate from the newly created droplet towards the nozzle and tends to slow down. This leads to a liquid metal column with an increasing length, trailing the nozzle as the printing progresses. After a critical length is reached, due to its own weight, the oxide skin encapsulating this column yields at the freeze front position leading to a distinct sag as shown in supporting information Fig. S1(a-b). Once we connect the horizontal section to the other vertical leg, a new freeze front emerges and completely freezes the structure and maintains the sagged shape. As such, experimental freeze front stagnation distance is determined through the optical measurement of the distance of the sagging point from the first vertical length. Although the stagnation distance (experimentally) could traverse further ±0.5 mm, with the present technology it was difficult to differentiate it from the sagging point.

4.3. The melting point of EGaIn

Alloys of Gallium and Indium exhibit the tendency to supercool [30]. Further, a wide range of gallium-indium alloy compositions have melting points near room temperature [31]. To determine the exact melting point of the prepared alloy (Ga – 78% and In – 22%), we conducted experiments in which we coated a thin layer of EGaIn on a Scotch Tape. The sample was then placed on a cold plate (TE Tech Inc. CP-121) and the temperature of the film was measured by the same procedure as mentioned above, neglecting thermal resistance between the film and thermistor. The cold plate temperature was slowly decreased from room temperature and the temperature at which freezing initiates (±1°C) is noted. The temperature was further lowered below the freezing point to about 8 °C after which the temperature was increased slowly. The temperature at which melting occurs is then noted (∼ 13 °C). The determined melting temperature was 13 ± 0.2 °C (thermistor accuracy is ±1°C). The complete experimental procedure is given in the supplementary information (Fig. S1(c)).

4.4. Ambient air temperature measurement

To study the ambient air temperature profile around the printed structure, a thermistor is attached in close proximity to the nozzle as shown in the supporting information (Fig. S2(a)). The ambient air profile is important to understand the convective heat transfer in the printed structure. The nozzle with the thermistor is translated from a close distance to the substrate film (0.5 mm) to a distance far away from the film (30 mm) in steps of 0.5 mm and the thermistor reading is recorded. Fig. 4 describes the experimentally measured temperature profile at 0 °C and 5 °C. In these measurements, we neglect the diametrical variation of temperature along the thermistor (diameter about 0.9 mm) and assume that the measured temperature is at the position of the central axis of the thermistor. The thermistor control range is from −40 °C to 70 °C and uses a 5k-1 TS-141 curve. To integrate these measurements into the model, we fitted cubic polynomials into the temperature distributions as a function of the distance (x) from the cold plate (Fig. 3).

4.5. Thermal conductivity measurement

The thermal conductivity of EGaIn is not well studied in the literature. Yu et al. [32] determined the thermal conductivity of liquid EGaIn from first principles at room temperature to be between 25 and 33 W/m-K. To the best of our knowledge, the thermal conductivity of solid EGaIn has not exclusively been studied before.

To determine the thermal conductivity of solid and liquid EGaIn in our working range of temperatures (0–30 °C) we measured the electrical resistivity of EGaIn at various temperatures and obtained

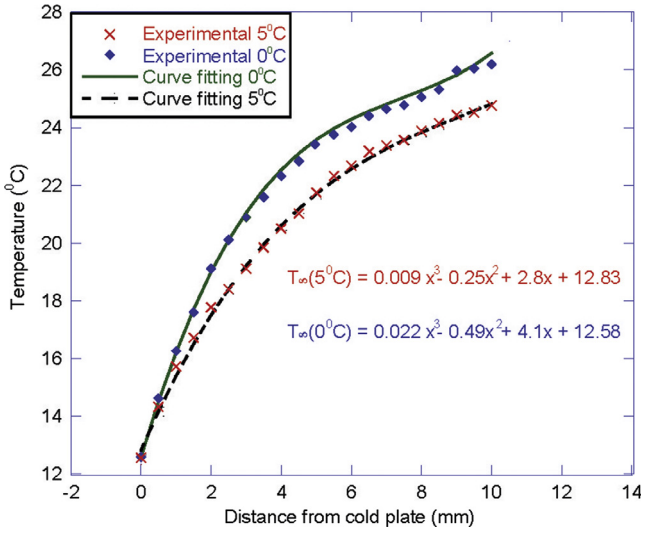

Fig. 3. Ambient temperature profile over the cold plate.

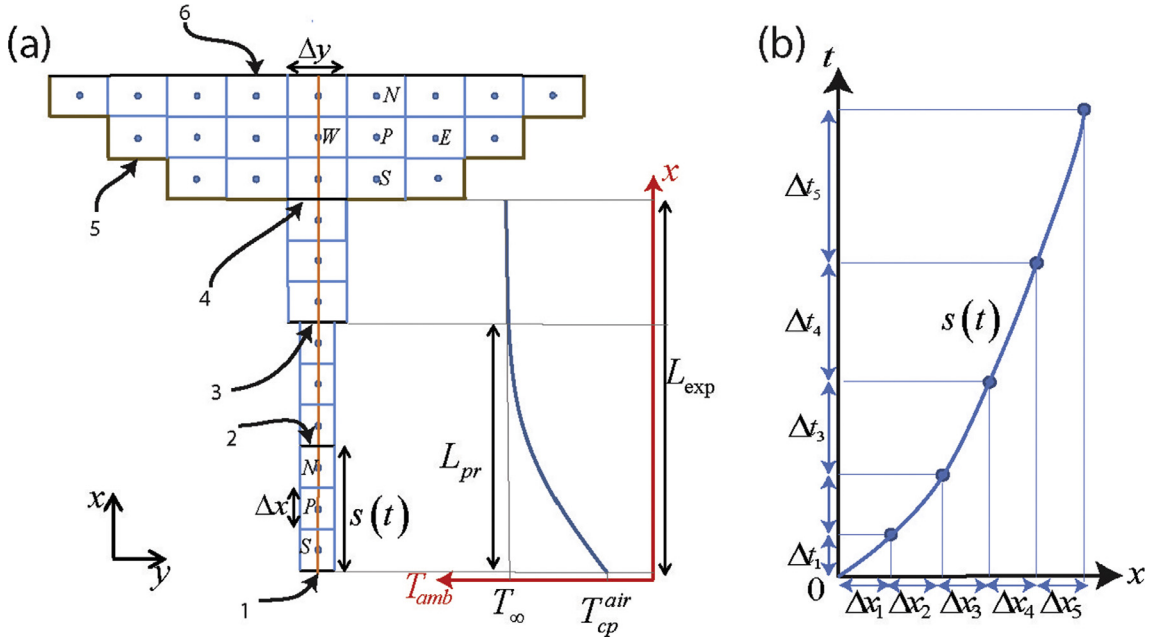

Fig. 4. (a) Control volume representation of the connected case. E, W, N and S represent the east, west, north and south grid points respectively across the grid of consideration P. In the reservoir we have 2D grids (E, W, S, N across P) and in the nozzle and printed structure we have 1D grids (N, S across P). Note that only three grids (along x) are chosen in each region (solid, liquid, nozzle and bulk) as representative elements in each section. The descriptions of the numeric labels are given in Table 1 below. Ambient temperature profile (T_∞) across the printed structure is plotted on the right. (b) Fixed grid variable time step.

electronic component of the thermal conductivity through Wiedemann-Franz law [19] as

$$K_e/\sigma T = \pi^2 \frac{\left(\frac{k_b}{e}\right)}{3} \tag{14}$$

where K_e is the electronic component of thermal conductivity (neglecting lattice contribution), σ is the electrical conductivity, T is the absolute temperature, k_B is Boltzmann's constant and e is the charge of an electron. For an alloy, the total thermal conductivity is the sum of electronic and lattice (K_f) thermal conductivity. The lattice thermal conductivity can be calculated using the Bridgman theory [33]. The value of K_f is nearly 1.65 W/m-K for EGaIn, an alloy having Ga-Ga interaction in dominance [32]. Hence the total conductivity for EGaIn is given by

$$K_t = K_e + K_f \tag{15}$$

The complete experimental procedure for thermal conductivity measurements is discussed in the supplementary information (Fig. S2(b)). To measure the electrical resistance, we chose a tube of 0.61 mm diameter (nominal 0.58 mm). To determine the variation in the tube diameter over the length of the tube (890 mm), after the electrical measurements, we analyzed the cross-section of the tube at different locations by cutting the tube that is filled with EGaIn. We observed a diameter variation of the tube from 0.59 mm to 0.62 mm across multiple sections. In this range, the thermal conductivity had a variation of ±1.2 W/m-K. Further, we used general purpose electrical wire at the two ends of the tube to facilitate measurements. The wire (~ 20 mm in length) resistance (~ 0.06Ω) and the interface resistance (~ 0.002Ω) have been subtracted prior to the measurement. Considering variations and uncertainty of various geometric and material parameters, within the working range of temperatures, we estimate the thermal conductivity for liquid EGaIn to be in the range of 25.5–28.9 W/m-K and that for the solid EGaIn to be in the range of 23–25 W/m-K. In the presented numerical model, the average values of these ranges were used.

5. Numerical solution

Close form analytical solution is impossible for the system described in freeze printing process. Thus, we have used a numerical technique to solve governing partial differential equations described in Section 3. A fully implicit finite volume based discretization is utilized because of its conservative flux balance on each control volume through its boundaries [34]. The position of the moving freeze front is determined by employing the modified variable-time-step approach described by Gupta and Kumar [18]. Fig. 4(a) and (b) show the uniform grid size and variable time steps used in this study. The total numbers of spatial grids considered were 5000 for the vertical printing with nozzle connected and horizontal cases and 3000 for nozzle disconnected case. The solution was invariant when the grids were increased further. In the modified variable-time-step approach, at any time t_n the time step Δt_n is so chosen that the interface (freeze front) moves exactly one grid in Δx in a time interval of Δt_n. This ensures that the freeze front always stays on the nodal boundary. Complete freezing of the printed structure is achieved when $m\Delta x = L_{pr}$, where m is the number of frozen grids and L_{pr} is the length of the printed structure as shown in Fig. 4(a). Stagnation of the freeze front is said to have reached when $\Delta t_n > 1500$ s or when the simulated time (t_n) reaches 6 min. Experimentally, we measured the freeze front position for 4–5 min after which we observed stagnation and oscillation of the freeze front at about the stagnation height. The freeze front motion with time is represented in Fig. 4(b). The solution is obtained either when there is complete freezing of the printed structure or stagnation of freeze front.

5.1. Discretized algebraic equations

5.1.1. Discretization equations for the solid, liquid and nozzle-liquid metal system

This section primarily presents algebraic equations for the cases A and C. The general form of the discretized equation for all the above-mentioned cases is given by

$$(a_P)_j^i (T_P)_j^i = (a_S)_j^i (T_S)_j^i + (a_N)_j^i (T_N)_j^i + b_j^i \quad i = s, l, eq \tag{16.1}$$

Here the subscript *P*, *S*, *N* represents the grid point in consideration at any location *x*, the grid to the south of grid *P*, and the grid to the north of grid *P* respectively. *b* is the source term in the discretization equation. The subscript *j* represents the j^{th} grid in the corresponding i^{th} region. Henceforth, the subscript *j* is dropped and the coefficients for various grids in the different regions are described. The coefficient definitions for discretization equations of the solid, liquid and nozzle-liquid alloy equivalent (*eq*) region are described in Table 2. The general form is as given in Eq. (16). The ambient temperature profile is given in Fig. 3 and the convective heat transfer coefficient can be found from Eqs. (9) and (10). The experimentally obtained material property values are presented in Table 4.

5.1.2. Discretization equations for the bulk metal in the syringe

The general form of discretization equations for the bulk region for cases A and C is given by

$$(a_P)(T_P) = (a_S)(T_S) + (a_N)(T_N) + (a_E)(T_E) + (a_W)(T_W) + b \tag{16.2}$$

Here the subscripts *P*, *S*, *N* take the same definition as above. *E*, *W* represents the east and the west grids respectively, to the grid point in consideration (*P*). To accurately represent the effect of liquid metal in the syringe, the heat transfer is modeled using 2-D heat equation given by Eq. (2). In discretizing the equation, owing to the symmetrical geometry of the syringe, nozzle and the printed structure, symmetry along the central axis can be realized as shown in Fig. 1(a). This symmetry simplifies the numerical solution in considering the nodal distribution only along one side of the central axis and mirroring its effect on the other. The various boundary conditions are given in Eqn. set 6 and are as represented in Fig. 4(a). Here, we assume that the temperatures of the east and the west grids are known prior to the calculation of the grid point in consideration (*P*).

5.1.3. Discretizing the interface energy balance equation

The interface energy balance equation is utilized to predict the time step required to freeze a grid on the printed structure. The discretized form of the equation is given by

$$(\Delta t)_n^i = \rho_{EGaIn} \frac{L h_f \Delta x^2}{2(k_s + k_l)} \left[\frac{1}{T_m - \left(\frac{k_s (T_{fn}^s)_n^i}{(k_s + k_l)} + \frac{k_l (T_1^l)_n^i}{(k_s + k_l)} \right)} \right] \tag{17}$$

In order to solve these set of discretized equations, the algorithm begins with an initial guess for temperatures for all the grids. The guessed value of the final grid (fn^{th} node) of the printed structure's solid grid and the 1st node of the liquid grid are used to calculate $(\Delta t)_n^i$ from the above equation. Here *i* represent the i^{th} iteration of $(\Delta t)_n$ which represents the time required to freeze the n^{th} grid in the printed sturcture. The $(\Delta t)_n^i$ value is then used to solve the discretized equations given in Table 2 and Table 3 iteratively using line-by-line tridiagonal matrix algorithm (TDMA) [37] until convergence of the nodal temperatures is achieved. At each iteration, the convective heat transfer coefficient (Eqs. (9) and (10)) is updated with the new temperature profiles. For quick convergence in this iterative scheme, an under-relaxation factor of 0.3 is used while updating the temperature profiles. Once converged, the new temperature information is then used to calculate $(\Delta t)_n^{i+1}$ and back substituted into the discretization equations described in Tables 2 and 3 until convergence of both temperature and time step is achieved. At this point, the solid grids are incremented by one, implying that the interface has moved one grid and algorithm is rerun to obtain the time step required to freeze another grid $(\Delta t)_{n+1}$. This is continued until the entire printed structure grids freeze or the time step required to freeze another grid exceeds 1500 s or the simulated time (summation of converged (Δt)) reaches 6 min at which the freeze front is determined to stagnate. This numerical algorithm used in this study is presented in Fig. 5.

Table 1
Description of the numeric labels in Fig. 4(a).

Label	Description
1	Cold Plate temperature boundary (Eq. (6.1))
2	Solid-liquid interface (Eq. (6.2))
3	Printed liquid-nozzle interface boundary (Eq. (6.3))
4	Nozzle-bulk transition boundary (Eq. (6.4))
5	Syringe-bulk metal interface (Eq. (6.5))
6	Mixed boundary at the top surface of the bulk (Eq. (6.6))

5.2. Case B: Nozzle disconnected

The discretization equations for the solid grids remain the same as the ones described for the connected case in Table 2. While the discretization equations of liquid grids change slightly due to the mixed boundary condition at the end of the printed structure. The only variation is that a_E is zero and a_{eff} is given by

$$(R_q)^l = \frac{((h_P) k_l / \Delta x)}{(h_P) + k_l / \Delta x} \tag{18}$$

The discretization equation for the interface energy balance equation is also as described in Eqs. (16.1) and (17).

The algorithm follows the same logic as described for the connected case. Iterative solver for the temperature profiles is not required here since the disconnected case is one dimensional and TDMA gives the direct solution. However, iterative solver for the time step is still required and follows the same procedure as described in Fig. 5.

6. Results and discussion

6.1. Results for various cases studied

To predict the steady-state freeze front position for the nozzle-connected (vertical printing) case, the discretization equations given in Table 2 and Table 3 are solved with the convective heat transfer profile as given in Eqs. (9) and (10). The liquid thermal conductivity (k_l) used in the model is 27 W/m-K and the solid thermal conductivity is 24 W/m-K as shown. The experimental and modeling results for the nozzle-connected vertical printing cases are given in Fig. 6(a) and (b) for different cold plate temperatures.

Here, one of the important parameters is the critical height (C_h) which is the steady-state vertical position of the freeze front prior to disconnection of the nozzle. As such, no structure printed in connection to a vertical line of length C_h can freeze and maintain structural stability during printing, which makes prediction of C_h critical towards process design. At 0 °C, the C_h experimentally determined to be 6 mm, as shown. The model predicts the critical height to be 7 mm. As we print higher line lengths, complete freezing of the line could not be realized prior to nozzle disconnection. The model successfully captures this behavior. At 5 °C, the experimental critical height is around 4 mm, while the model predicts it ~5 mm. As we print longer lines, the model deviates from the experimental data. Possible reasons for the discrepancies are discussed below.

For the nozzle disconnected vertical printing case, the model results match closely with the experimental observation for both 0 °C and 5 °C cold plate temperature as shown in Fig. 6(c). Experimentally, at 0 °C the printed line completely freezes until 11 mm and for higher line lengths, the freeze front (FF) position drops as length increases. This variation is accurately predicted by the

Table 2
Set of discretization equations for solid, liquid and nozzle-liquid metal system.

General form of discretization equation (Eq. (16.1))		a_P	a_N	a_S	b
Discretization equation of solid grid when there is only 1 solid grid		$2(a_b)^s + (a_P)_o^s + (h_P)\Delta x$	0	0	$(a_P)_o^s(T_P)_o^s + (a_b)^s(T_{cp} + T_m) + (h_P)(T_{air})\Delta x$
Discretization equations of solid grids when there are more than 1 solid grid	West boundary grid	$(a_b)^s + (a_N)^s + (a_P)_o^s + (h_P)\Delta x$	$\frac{k_s}{\Delta x}$	0	$(a_P)_o^s(T_P)_o^s + (a_b)^s T_{cp} + (h_P)(T_{air})\Delta x$
	Central grids	$(a_N)^s + (a_S)^s + (a_P)_o^s + (h_P)\Delta x$	$\frac{k_s}{\Delta x}$	$\frac{k_s}{\Delta x}$	$(a_P)_o^s(T_P)_o^s + (h_P)(T_{air})\Delta x$
	East boundary grid	$(a_b)^s + (a_S)^s + (a_P)_o^s + (h_P)\Delta x$	0	$\frac{k_s}{\Delta x}$	$(a_P)_o^s(T_P)_o^s + (a_b)^s T_m + (h_P)(T_{air})\Delta x$
Discretization equations of liquid grids	West boundary grid	$(a_b)^l + (a_N)^l + (a_P)_o^l + (h_P)\Delta x$	$\frac{k_l}{\Delta x}$	0	$(a_P)_o^l(T_P)_o^l + (a_b)^l T_m + (h_P)(T_{air})\Delta x$
	Central grids	$(a_N)^l + (a_S)^l + (a_P)_o^l + (h_P)\Delta x$	$\frac{k_l}{\Delta x}$	$\frac{k_l}{\Delta x}$	$(a_P)_o^l(T_P)_o^l + (h_P)(T_{air})\Delta x$
	East boundary grid	$(a_{eff}) + (a_S)^l + (a_P)_o^l + (h_P)\Delta x$	a_{eff}	$\frac{k_l}{\Delta x}$	$(a_P)_o^l(T_P)_o^l + (h_P)(T_{air})\Delta x$
Discretization equations of the nozzle-liquid metal system	West boundary grid	$(a_{eff}) + (a_N)^{eq} + (a_P)_o^{eq} + (h_P)\Delta x$	$\frac{k_{eq}}{\Delta x}$	a_{eff}	$(a_P)_o^{eq}(T_P)_o^{eq} + (h_P)(T_{air})\Delta x$
	Central grids	$(a_N)^{eq} + (a_S)^{eq} + (a_P)_o^{eq} + (h_P)\Delta x$	$\frac{k_{eq}}{\Delta x}$	$\frac{k_{eq}}{\Delta x}$	$(a_P)_o^{eq}(T_P)_o^{eq} + (h_P)(T_{air})\Delta x$
	East boundary grids	$(a_{eff}) + (a_S)^{eq} + (a_P)_o^{eq} + (h_P)\Delta x$	(a_{eff})	$\frac{k_{eq}}{\Delta x}$	$(a_P)_o^{eq}(T_P)_o^{eq} + (h_P)(T_{air})\Delta x$
Variable definitions used in this table		$(a_b)^i = \frac{k_i}{(\Delta x/2)} \quad i = s, l$	$a_{eff} = \frac{k_l k_{eq}}{(k_l + k_{eq})}\frac{1}{\Delta x}$		$(a_P)_o^i = \frac{\rho_i C_i \Delta x}{(\Delta t)^n} \quad i = s, l, eq$

Table 3
Set of discretization equations for the bulk metal in the syringe.

General form of discretization equation (Eq. (16.2))	a_P	a_N	a_S	b
Discretization equation of west boundary grid on central axis	$(a_{eff})\Delta y + (a_N) + (a_P)_o$	$\frac{k_l}{\Delta x}\Delta y$	$(a_{eff})\Delta y$	$2(a_E)(T_E) + (a_P)_o(T_P)_o$
Discretization equation of internal grids on central axis	$(a_N) + (a_S) + (a_P)_o + 2(a_E)$	$\frac{k_l}{\Delta x}\Delta y$	$\frac{k_l}{\Delta x}\Delta y$	$(a_P)_o(T_P)_o + 2(a_E)(T_E)$
Discretization equation of east boundary grid on central axis	$(R_q) + (a_S) + (a_P)_o + 2(a_E)$	0	$\frac{k_l}{\Delta x}\Delta y$	$(R_q)T_{in} + (a_P)_o(T_P)_o + 2(a_E)(T_E)$
Discretization equation of northwest boundary grid	$(a_N) + (a_W) + (a_P)_o$	$\frac{k_l}{\Delta x}\Delta y$	0	$(a_P)_o(T_P)_o + (a_W)(T_W)$
Discretization equation of northeast boundary grid	$(R_q) + (a_W) + (a_P)_o + (a_S)$	0	$\frac{k_l}{\Delta x}\Delta y$	$(R_q)T_{in} + (a_P)_o(T_P)_o + (a_W)(T_W)$
Discretization equation of the remaining north boundary grids	$(a_N) + (a_W) + (a_P)_o + (a_S)$	$\frac{k_l}{\Delta x}\Delta y$	$\frac{k_l}{\Delta x}\Delta y$	$(a_P)_o(T_P)_o + (a_W)(T_W)$
Discretization equation of the remaining west boundary grids	$(a_E) + (a_N) + (a_P)_o + (a_W)$	$\frac{k_l}{\Delta x}\Delta y$	0	$(a_E)(T_E) + (a_W)(T_W) + (a_P)_o(T_P)_o$
Discretization equation of the remaining east boundary grids	$(R_q) + (a_W) + (a_P)_o + (a_S) + (a_E)$	0	$\frac{k_l}{\Delta x}\Delta y$	$(R_q)T_{in} + (a_P)_o(T_P)_o + (a_W)(T_W) + (a_E)(T_E)$
Discretization equation of the internal grids in bulk	$(a_E) + (a_W) + (a_P)_o + (a_S) + (a_N)$	$\frac{k_l}{\Delta x}\Delta y$	$\frac{k_l}{\Delta x}\Delta y$	$(a_E)(T_E) + (a_W)(T_W) + (a_P)_o(T_P)_o$
Variable definitions used in the table	$(a_N) = (a_S) = \frac{k_l \Delta x}{\Delta y}$	$(a_P)_o = \frac{\rho_{bulk} C_{bulk} \Delta x \Delta y}{(\Delta t)^n}$		$(R_q) = \frac{(\langle h_{still}\rangle k_l/\Delta x)}{(h_{still}) + k_l/\Delta x}\Delta y$

Table 4
Property values used for the numerical results [35,32,31,21,36].

EGaIn	$\rho_{EGaIn} = 6250\frac{kg}{m^3}$	$Lh_f = 67100\frac{J}{kg}$	$C_{EGaIn} = 310\frac{J}{kgK}$	–
Steel	$\rho_{steel} = 7500\frac{kg}{m^3}$	–	$C_{steel} = 500\frac{J}{kgK}$	$k_{steel} = 26\frac{W}{mK}$
Air	$\rho_{air} = 1.205\frac{kg}{m^3}$	–	$C_{air} = 1005\frac{J}{kgK}$	$k_{air} = 0.025\frac{W}{mK}$
	$\upsilon_{air} = 0.142 \times 10^{-4}\frac{m^2}{s}$	$\beta_{air} = 0.00343K^{-1}$	$Pr_{air} = 0.71$	

model as shown in the figure. For 5 °C, the model predicts the freeze front position of the printed line accurately until complete freezing but slightly underestimates for lines where the freeze front stagnates. Reasons for which are discussed below.

For the horizontal printing, four cases involving horizontal line lengths of 10 mm, 16 mm, 18 mm and 20 mm printed over a vertical line of 5 mm length were considered. The average horizontal diameters of the printed lines were 150 μm, 160 μm, 200 μm and 200 μm respectively. As shown in Fig. 6(d) the model predicts closely with the experimental data with a variation of ±1 mm.

6.2. Discussions on the model-experiment discrepancies

In general our model successfully captured the behavior of the freeze front during freeze-printing. The observed discrepancies can be due to a number of reasons:

- The measurement of the ambient temperature profile was performed using a thermistor probe of non-negligible size. As such, the temperature measured at a given elevation is an averaged value across the thermistor probe tip, potentially causing deviations in the temperature profile.
- The freeze printing process starts with a formation of a droplet and its contact to the substrate surface. As such, the printed vertical lines include a short section with increased diameter right at the substrate. This region was omitted in the model for simplicity. In the horizontal printing case, the horizontal line is connected to the vertical line in a similar fashion, causing added potential discrepancies.
- The variations of material properties, particularly the thermal conductivity were neglected in this study.
- For the nozzle-connected and the horizontal printing cases, the consideration of equivalent nozzle-liquid metal system disre-

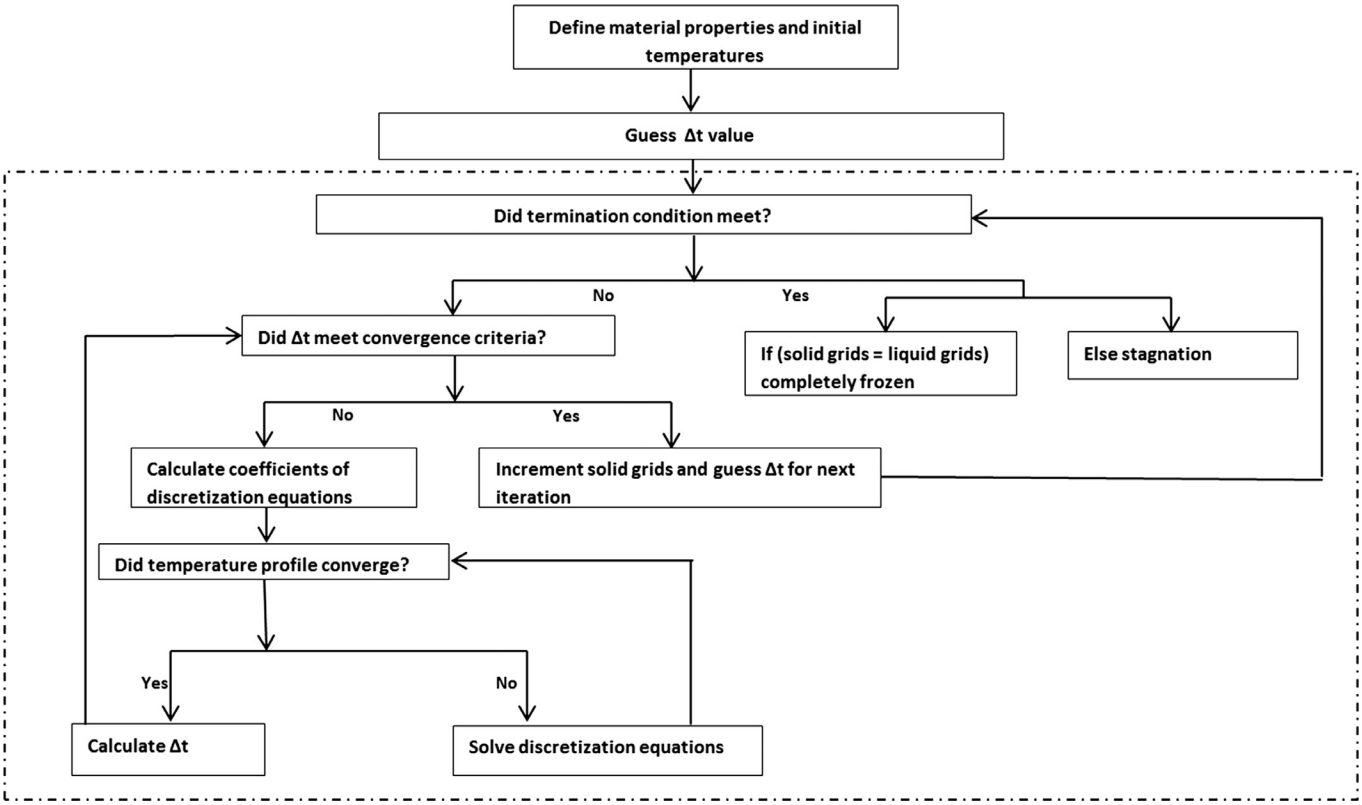

Fig. 5. Flow chart of the algorithm.

gards the interfacial thermal phenomena between the nozzle and the liquid metal. Furthermore, the stainless steel nozzles have a passivation coating on their outer surface. This layer being thermally less conductive than stainless steel decreases the effect of convective heating from across the nozzle (ambient air is hotter than the printed structure) and into the printed structure, but is being neglected for simplicity.

- During the experiments, we observed that freeze front tends to oscillate around a steady state position especially at higher elevations from the cold plate (see Supplementary Video). This can be due to (1) temporal variations of the ambient temperatures, (2) errors in material preparation leading to alloys with non-eutectic compositions and thus exhibiting a "mushy" state in between the solidus and liquidus boundaries, as observed in many other alloys [38].
- The horizontal lines exhibited higher diameter variations, within a single line compared to the vertical lines. For the model, an average diameter was considered, which may lead to discrepancies. The main reason behind this diameter variation is the complex, oxide skin deformation dependent flow and deposition mechanism of freeze-printing, which is beyond the scope of this study. Furthermore, the experimental freeze front position was noted to be the point of sagging as shown in Fig. S1(a)-(b). Since this determination relies on our visual observation and estimate on the exact sagging point, loss of accuracy is expected. These reasons might account for the discrepancies between the model and experiments observed in Fig. 6(d).
- We also observed that the lighting that is used during experimentation to provide better visual observation for freeze front position determination caused variations in the freeze front position (±0.2mm). This can be associated with the increased radiative heat transfer due to the incident light and is neglected in this analysis.

6.3. Discussions on the critical findings of the study

The critical conclusions that can be drawn from the presented experimental and modeling results are summarized below:

- Natural convection for low Grashof numbers is not well studied in the literature. Most of the studies on natural convection are in the range of $10^5 < Gr < 10^9$. At low Grashof numbers, shape factor, which is the surface area to volume ratio, and slenderness (L/D) ratio, is an important factor governing convective heat transfer. The boundary layer assumptions that are generally valid for higher Grashof numbers are not applicable for low Grashof numbers. To address this, the present work proposes a modified formulation by introducing an additive constant (A) in the Nusselt number equation to account for the shape factors. This leads to a higher Nusselt number than that we observe in natural convection for high Grashof numbers. This higher Nusselt numbers could be due to the increased surface effects (convective heating) and decreased cross-sectional effects (conductive heating) due to the high slenderness (L/D) of the printed structures.
- This work presents a quasi-1D heat equation, which takes into account the boundary convective effects as a distributed heat source in the governing differential equations. As demonstrated in this work, this approximation is a fairly good assumption for slender geometries (high L/D) and for highly conductive materials such as in the present case.

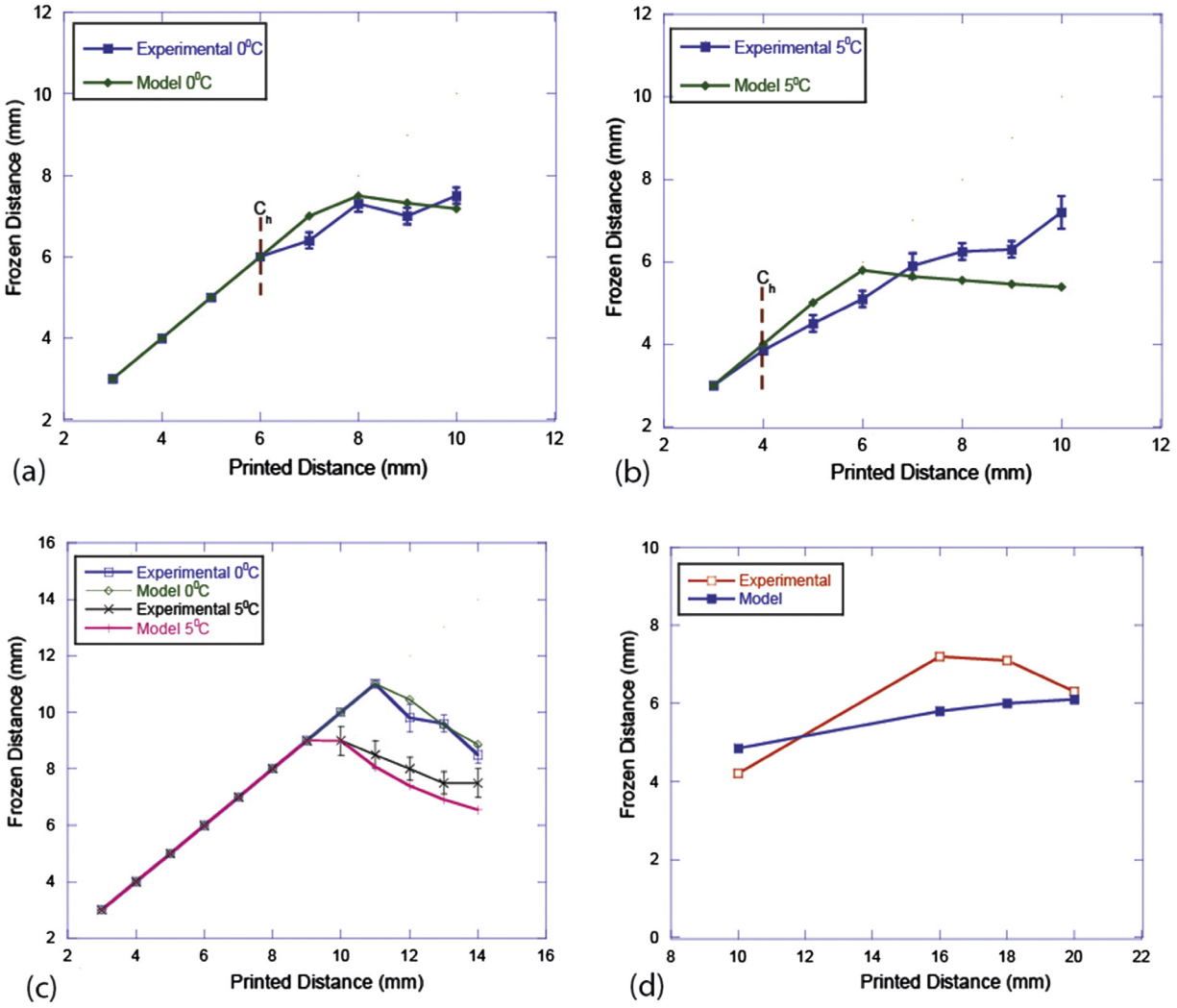

Fig. 6. Experimental and numerical results for vertical printing (a)-(b) nozzle-connected case, (c) nozzle-disconnected case, and (d) horizontal printing case. In (a-c), the experimental data points are an average of 5 tests at each vertical length with nozzle connected and disconnected configuration. The error bars are the variation from the mean value under different tests (<5%).

- Experimental-model results in Fig. 6 indicate that the effect of convection increases with the increase in line lengths. To elaborate, if the process was conduction dominant (negligible convective heating) then the expected temperature variation will be linear in line length between the nozzle and the cold plate. Under the same boundary conditions, this would imply that at any location above the cold plate, the temperature would decrease with increasing line length and thus the steady state freeze front position would rise with line lengths. This is in contradiction to our experimental observations. This is particularly interesting as for low Grashof numbers, such as the present case ($Gr < 5 \times 10^3$), heat transfer is known to be conduction dominant [28].
- The solid thermal conductivity is lower than the liquid thermal conductivity for EGaIn, indicating a possible drop in density when the metal freezes. Further, we identified the solid thermal conductivity within 0–13 °C to be around 23 W/m-K – 25 W/m-K.

7. Conclusion

In the present investigation, we developed a thermal model for the prediction of the steady-state freeze front position of our 3D freeze printing based additive manufacturing technique. In this regard, we studied the dependence of freeze front position of the printed structure on the cold plate temperature and the structure geometry. We experimentally measured the steady state freeze front position and modeled its response through the consideration of conductive and convective heat transfer as well as thermal mechanisms of phase change. We considered two different cold plate temperatures – 0 °C and 5 °C. We introduce a quasi 1D governing equation for energy in which the convective boundary condition is integrated within the differential equation. Model results match closely with experimental data for the different cases we considered, namely, (a) nozzle connected vertical printing case (b) nozzle disconnected vertical printing case and (c) horizontal line printing case. These results particularly indicate that (1) the thermal conductivity of the liquid metal of interest was accurately characterized, (2) quasi 1-D or fin equation consideration in modeling heat transfer on slender cylindrical geometries is justified, (3) selection of the particular convective heat transfer model is valid for the demonstrated size scales and thermal conditions

This work is the first of kind in the literature towards a complete thermal analysis of the continuous direct-writing-based additive manufacturing of metallic structures. The outcomes of this model such as the critical height determination can be used to

make important design decisions regarding the part and the process design. The present model can be used to study the freeze-printing process involving any metal of known thermophysical properties. Our current efforts focus on the printing of low-melting point metals including Field's metal (m.p 70 °C). The future work regarding the modeling efforts will primarily include, (1) betterment of the current model by incorporating the aforementioned neglected phenomena and (2) improving it to capture transient freeze front position while printing. This improved model will help us make a critical decision on the usable printing speeds, directly impacting the throughput of the freeze-printing process.

Acknowledgements

The authors acknowledge the funding from the WSU New Faculty Seed Grant 2015 (Grant # 125627).

Conflict of interest

The authors declare that there is no conflict of interest.

Appendix A. Supplementary material

Supplementary data associated with this article can be found, in the online version, at http://dx.doi.org/10.1016/j.ijheatmasstransfer.2017.07.092.

References

[1] B.Y. Ahn et al., Omnidirectional printing of flexible, stretchable, and spanning silver microelectrodes, Science(80-) 323 (2009) 1590–1593.
[2] R.K. Kramer, Soft Electron. Soft Robot. 9467 (2015) 946707.
[3] H. Yang, M.T. Rahman, D. Du, R. Panat, Y. Lin, 3-D printed adjustable microelectrode arrays for electrochemical sensing and biosensing, Sens. Actuat., B Chem. 230 (2016) 600–606.
[4] Y. Zheng, Z.-Z. He, J. Yang, J. Liu, Personal electronics printing via tapping mode composite liquid metal ink delivery and adhesion mechanism, Sci. Rep. 4 (2014) 4588.
[5] S. Felton, M. Tolley, E. Demaine, D. Rus, R. Wood, A method for building self-folding machines, Science(80-) 345 (2014) 644–646.
[6] A. Mette, P.L. Richter, M. Horteis, S.W. Glunz, Metal aerosol jet printing for solar cell metallization, Prog. Photovolt Res. Appl. 15 (2007) 659–676.
[7] Kenry, J.C. Yeo, C.T. Lim, Emerging flexible and wearable physical sensing platforms for healthcare and biomedical applications, Microsyst. Nanoeng. 2 (2016) 16043.
[8] J. Scott, N. Gupta, C. Weber, S. Newsome, Additive manufacturing: Status and opportunities, Sci. Technol. Policy Inst. 1–35 (2012).
[9] S.-P. Chen, H.-L. Chiu, P.-H. Wang, Y.-C. Liao, Inkjet printed conductive tracks for printed electronics, ECS J. Solid State Sci. Technol. 4 (2015) P3026–P3033.
[10] T. Rahman et al., Structure, electrical characteristics, and high-temperature stability of aerosol jet printed silver nanoparticle films, J. Appl. Phys. 75305 (2016).
[11] J.W. Boley, E.L. White, G.T.-C. Chiu, R.K. Kramer, Direct writing of gallium-indium alloy for stretchable electronics, Adv. Funct. Mater. n/a-n/a (2014), http://dx.doi.org/10.1002/adfm.201303220.
[12] J. Hu, M.-F. Yu, Meniscus-confined three-dimensional electrodeposition for direct writing of wire bonds, Science (80-) 329 (2010) LP313–LP316.
[13] M.A. Skylar-Scott, S. Gunasekaran, J.A. Lewis, Laser-assisted direct ink writing of planar and 3D metal architectures, Proc. Natl. Acad. Sci. 113 (2016) 201525131.
[14] A. Gannarapu, B.A. Gozen, Freeze-printing of liquid metal alloys for manufacturing of 3D, conductive, and flexible networks, Adv. Mater. Technol. (2016), http://dx.doi.org/10.1002/admt.201600047.
[15] W.E. Frazier, Metal additive manufacturing: a review, J. Mater. Eng. Perform. 23 (2014) 1917–1928.
[16] S.M. Kelly, S.L. Kampe, Microstructural evolution in Laser-Deposited multilayer Ti6Al-4V build: Part I. Microstructural characterization, Metall. Mater. Trans. A 35 (2004) 1861–1867.
[17] S.M. Kelly, S.L. Kampe, Microstructural evolution in laser-deposited multilayer Ti-6Al-4V builds: Part II Thermal modeling, Metall. Mater. Trans. A 35 (2004) 1861–1867.
[18] R.S. Gupta, D. Kumar, Variable time step methods for one-dimensional Stefan problem with mixed boundary condition, Int. J. Heat Mass Transf. 24 (1981) 251–259.
[19] G.V. Chester, A. Thellung, The law of Wiedemann and Franz, Proc. Phys. Soc. 77 (1961) 1005–1013.
[20] C. Ladd, J.-H. So, J. Muth, M.D. Dickey, 3D printing of free standing liquid metal microstructures, Adv. Mater. 25 (2013) 5081–5085.
[21] M.D. Dickey, Emerging applications of liquid metals featuring surface oxides, ACS Appl. Mater. Interfaces 6 (2014) 18369–18379.
[22] F. Scharmann et al., Viscosity effect on GaInSn studied by XPS, Surf. Interface Anal. 36 (2004) 981–985.
[23] K.A. Gardner, Efficiency of extended surfaces, Trans. ASME 67 (1945) 621–631.
[24] A.G. Lyapin, E.L. Gromnitskaya, O.F. Yagafarov, O.V. Stalgorova, V.V. Brazhkin, Elastic properties of crystalline and liquid gallium at high pressures, J. Exp. Theor. Phys. 107 (2008) 818–827.
[25] T.W. Richards, S. Boyer, Further studies concerning gallium, 1540 (1919).
[26] S.W. Churchill, H.H.S. Chu, Correlating equations for laminar and turbulent free convection from a vertical plate, Int. J. Heat Mass Transf. 18 (1975) 1323–1329.
[27] E.J. LeFevre, Laminar free convection from a vertical plane surface, in: Proc. 9th Int. Congress Applied Mechanics 4 (1956) 168–174.
[28] J.H.L. Iv, J.H. Lienhard, A heat transfer textbook, J. Heat Transf. 108 (1986) 198.
[29] G. Windsor, Observation of a metastability limit in liquid gallium, Phys. Rev. Lett. 1652–1655 (1975).
[30] G. Windsor, Observation of a Metastability Limit in Liquid Gallium (1975) 1652–1655.
[31] W.J. Svirbely, S.M. Selis, The gallium-indium system, J. Phys. Chem. 58 (1954) 33–35.
[32] S. Yu, M. Kaviany, Electrical, thermal, and species transport properties of liquid eutectic Ga-In and Ga-In-Sn from first principles, J. Chem. Phys. 140 (2014) 1–8.
[33] P.W. Bridgman (Percy W. & 1882-1961), The Physics of High Pressure, 1952.
[34] H.K. Versteeg, W. Malalasekera, An introduction to computational fluid dynamics, World Wide Web Inter. Web Inform. Syst. 1 (2007).
[35] M.D. Dickey et al., Eutectic Gallium-Indium (EGaIn): a liquid metal alloy for the formation of stable structures in microchannels at room temperature, Adv. Funct. Mater. 18 (2008) 1097–1104.
[36] J.C. Dixon, Appendix B: Properties of Air, Shock Absorber Handbook 375–378.
[37] S.V. Patankar, Numerical heat transfer and fluid flow, Ser. Coputat. Meth. Mech. Therm. Sci. 1–197 (1980), http://dx.doi.org/10.1016/j.watres.2009.11.010.
[38] M.G. Worster, Instabilities of the liquid and mushy regions during solidification of alloys, J. Fluid Mech. 237 (1992) 649–669.